

Tomography-based monitoring of isothermal snow metamorphism under advective conditions

Pirmin Philipp Ebner^{1,2}, Martin Schneebeli^{2,*}, and Aldo Steinfeld^{1,*}

¹ *Department of Mechanical and Process Engineering, ETH Zurich, 8092 Zurich, Switzerland*

² *WSL Institute for Snow and Avalanche Research SLF, 7260 Davos-Dorf, Switzerland*

Abstract

Time-lapse X-ray microtomography was used to investigate the structural dynamics of isothermal snow metamorphism exposed to an advective airflow. The effect of diffusion and advection across the snow pores on the snow microstructure were analysed in controlled laboratory experiments and possible effects on natural snowpacks discussed. The 3D digital geometry obtained by tomographic scans was used in direct pore-level numerical simulations to determine the effective permeability. The results showed that isothermal advection with saturated air have no influence on the coarsening rate that is typical for isothermal snow metamorphism. Isothermal snow metamorphism is driven by sublimation-deposition caused by the Kelvin effect and is the limiting factor independently of the transport regime in the pores.

Keywords: snow, isothermal, metamorphism, advection, transport properties, tomography

1. Introduction

Snow is a bi-continuous material consisting of fully connected ice and pore space (air) (Löwe et al. 2011). Because of the proximity to the melting point, the high vapour pressure causes a continuous recrystallization of the snow microstructure known as snow metamorphism, even under moderate temperature gradients (Pinzer et al, 2012; Domine et al. 2008). The microstructural changes of snow towards equilibrium under conditions of constant temperature are referred to as isothermal snow metamorphism

* Corresponding author. Email: aldo.steinfeld@ethz.ch and schneebeli@slf.ch

29 (Colbeck, 1997; Kaempfer and Schneebeli, 2007). This is a coarsening process whose
30 driving force is the reduction of the surface free energy of the complex ice-air interface.
31 The energy reduction is caused by mass transport processes such as vapour diffusion
32 (Neumann et al., 2009), surface diffusion (Kingery, 1960b), volume diffusion (Kuroiwa,
33 1961), and grain boundary diffusion (Colbeck, 1997a, 1998, 2001; Kaempfer and
34 Schneebeli, 2007). Viscous or plastic flow (Kingery, 1960a), and sublimation-
35 condensation with vapour transport (German, 1996; Hobbs and Mason, 1963; Lega-
36 gneux and Domine, 2005; Maeno and Ebinuma, 1983) are also suggested to play an im-
37 portant role. The Kelvin effect is seen as the driving force for isothermal snow meta-
38 morphism (Bader, 1939; Colbeck, 1980). Recent studies indicate that sublimation-
39 deposition is the dominant contribution for temperatures close to the melting point,
40 whereas surface diffusion dominates at temperatures far below the melting point (Vetter
41 et al, 2010). Snow has a high permeability, which facilitates diffusion of gases and, un-
42 der appropriate conditions, airflow (Gjessing, 1977; Colbeck, 1989; Sturm and Johnson,
43 1991; Waddington et al., 1996). Both diffusion and advective airflow affect heat and
44 mass transports in the snowpack (Cunningham and Waddington, 1993; Albert, 1993;
45 McConnell et al. 1998). In the dry snow zone of an ice sheet, Sowers et al. (1992) de-
46 scribed a convective zone located just below the surface in which the air is rapidly
47 flushed by convective exchange with the overlying atmosphere. A rapid decrease of the
48 airflow velocity inside a snow layer ($\leq 0.01 \text{ m s}^{-1}$) for high wind speed ($\approx 10 \text{ m s}^{-1}$)
49 above the snow surface (pore size $\approx 1 \text{ mm}$) are numerically estimated by Neumann
50 (2003). In addition, Colbeck et al. (1997) confirmed the rapid decrease of airflow veloci-
51 ties inside a snowpack. Advective flow of air may have a direct effect on snow-air ex-
52 change processes related to atmospheric chemistry (Clifton et al., 2008; Grannas et al.,
53 2007), and snow metamorphism (Albert and Gilvary, 1992; Albert et al., 2004), and can
54 change the chemical composition of trapped atmospheric gases in ice-cores (Legrand
55 and Mayewski, 1997; Neumann and Waddington, 2004; Severinghaus et al., 2010).
56 However, no prior studies have experimentally analyzed the effect of saturated airflow
57 on the vapour transport and the recrystallization of the snow crystals using non-
58 destructive technique in time-lapse experiments. Over- or undersaturated air leads to a
59 rapid growth or shrinkage of snow structures exposed to such conditions, as exemplified
60 in the growth of surface hoar (Stössel et al., 2010). However, saturation vapour density
61 of the air is reached in the pore space within the first 1 cm of the snow sample, regard-

62 less of temperature or flow rate (Neumann et al., 2009; Ebner et al., 2014). The change
63 in shape of the snow crystals during metamorphism also affects the permeability, which,
64 in turn, will continue to affect the shape of the snow structure. Although long-term iso-
65 thermal metamorphism occurs in nature only in the centre of the polar ice caps (Arnaud
66 et al., 1998), it is important to reduce physical complexity of experiments in order to
67 understand the basic mechanisms governing metamorphism.

68 The objective of this paper is to study the effect of saturated airflow on the vapour
69 transport and the coarsening rate of snow under isothermal conditions. We designed ex-
70 periments in a controlled refrigerated laboratory and used time-lapse computed tomog-
71 raphy (micro-CT) to obtain the discrete-scale geometry of snow (Schneebeli and Sokra-
72 tov, 2004; Kaempfer and Schneebeli, 2007; Pinzer and Schneebeli, 2009; Chen and
73 Baker, 2010; Pinzer et al., 2012; Wang and Baker, 2014; Ebner et al., 2014). The ex-
74 tracted 3-D digital geometry of the snow was used to calculate the specific surface area
75 and porosity. Direct pore-level simulations (DPLS) were applied to determine the effec-
76 tive permeability by solving the corresponding mass and momentum conservation equa-
77 tions (Zermatten et al., 2011, 2014).

78 **2. Methodology**

79 Isothermal experiments with fully saturated airflow across snow samples were per-
80 formed in a micro-CT at laboratory temperatures of $T_{\text{lab}} = -8$ and -15 °C. Figure 1
81 shows a schematic of the experimental setup (Ebner et al., 2014). It is to be noticed that
82 the accurateness of the isothermal conditions between the top and base of the sample
83 was less than 0.2 °C and a temperature gradient of about 6.7 K m^{-1} was possible. How-
84 ever, this was still in the uncertainty of the thermistors $\pm 0.2 \text{ K}$ (Ebner et al., 2014) and
85 therefore a quasi-isothermal condition was given. Two different snow types with high
86 specific surface area were considered to evaluate the structural change in the earlier
87 stage of isothermal metamorphism of new snow, more in detail. Partly decomposed
88 snow (DFdc) was used for low flow rate ('sa1' and 'sa2') whereas large rounded snow
89 (RGlR) was used for higher flow rate ('sa3' and 'sa4') to prevent destruction of the frag-
90 ile snow structure (Fierz et al., 2009). Nature identical snow was used for the snow
91 sample preparation (water temperature: 30 °C; air temperature: -20 °C) (Schleef et al.,
92 2014). It was sieved with a mesh size of 1.4 mm into two boxes, and sintered for 13 and
93 27 days at -15 and -5 °C, respectively, for increasing strength and coarsening

94 (Kaempfer and Schneebeli, 2007). A cylinder cut out (diameter: 53 mm; height: 30 mm)
95 from the sintered snow was filled into the sample holder (Ebner et al., 2014). The snow
96 samples were analysed during 96 h with time-lapse micro-CT measurements taken every
97 8 h, producing a sequence of 13 images. Table 1 summarizes the morphological parame-
98 ters of the snow. Four different runs were chosen based on the Peclet number ($Pe =$
99 $u_D d_p / D$ where u_D is the superficial velocity in snow, d_p is the pore diameter, and $D =$
100 $2.036 \cdot 10^{-5} \text{ m}^2 \text{ s}^{-1}$ is the diffusion coefficient of water vapour in air) to compare the ad-
101 vective and diffusive transport rates inside the pore space. Experimental runs were per-
102 formed at 1 atm pressure and volume flow rates of 0 (no advection), 0.36, 3.0, and 5.0 L
103 min^{-1} , corresponding to $Pe = 0, 0.05, 0.47,$ and 0.85 . Higher Pe numbers were experi-
104 mentally not possible, as the shear stress by airflow could destroy the snow structure and
105 we restricted the flow rate to the corresponding maximum $Pe \approx 0.8$ extracted from the
106 simulations of Neumann (2003) and Colbeck (1997). Assuming an isothermal snow-
107 pack, $Pe > 1$ is unlikely in nature because of: 1) low density snow, which has always a
108 very low strength, will be destroyed due to the high airflow velocity; 2) Pe depends on
109 the temperature due to changing diffusivity. Seasonal temperature fluctuations of -60°C
110 to -30°C are typical for surface snow layer in Antarctic regions, and lead to Pe varia-
111 tions of up to 25%. Theoretically, $Pe \approx 1.2$ could be realistic at -60°C for a superficial
112 velocity of $\approx 0.06 \text{ m s}^{-1}$ (experiment ‘sa4’). However, simulations by Neumann (2003)
113 showed a rapid decrease of the airflow velocity inside the snow layer ($\leq 0.01 \text{ m s}^{-1}$) for a
114 high wind speed ($\approx 10 \text{ m s}^{-1}$) above the snow surface (pore size $\approx 1 \text{ mm}$). This leads to a
115 maximum $Pe \approx 0.8$. 3) $Pe > 1$ would be possible for depth hoar, but this snow type is
116 typically found at depth and rarely exposed to high windspeed (Colbeck, 1997). Depth
117 hoar founded close to the surface (Alley et al., 1990; Gallet et al., 2014) were formed
118 under light winds conditions. According to the reported Beaufort number (in Alley et al.,
119 1990), this will be a maximum wind speed of $\approx 2\text{-}3 \text{ m s}^{-1}$ (see also Gallet et al., 2014)
120 above the surface. In addition, the depth hoar developed in the slopes of older dunes,
121 leading to an additional decrease of the actual wind speed ($\approx 1 \text{ m s}^{-1}$) above the depth
122 hoar layer. Based on the simulations of Neumann (2003) an airflow velocity inside the
123 depth hoar of $\leq 0.002 \text{ m s}^{-1}$ would be realistic. To reach a Peclet number > 1 under this
124 condition, the mean pore size must be at least 10 mm, which would be a very extreme
125 case for depth hoar formed close to the surface. Additionally, Adams and Walters
126 (2014) showed that the top layer of such depth hoar consists of long slender needle crys-

127 tals connected in a cross-hatch pattern which has a low strength and will be destroyed by
128 such a strong flow.

129 The acceleration voltage in the X-ray tube was 70 kV, with an intensity of 114 μA ,
130 and a nominal resolution of 18 μm . The samples were scanned with 2000 projections
131 per 360 degree, with an integration time of 200 ms per projection, taking 1.5 hour per
132 scan. The innermost 36.9 mm of the total 53 mm diameter were scanned and subsamples
133 with a dimension of $7.2 \times 7.2 \times 7.2 \text{ mm}^3$ were extracted for further processing. Absolute
134 z -position varied up to a maximum of 50 voxels between subsequent scans due to the
135 weight of the sample holder. To correct for the z -position a linear encoder was built into
136 the micro-CT. A $3 \times 3 \times 3$ median filter and Gaussian filter ($\sigma = 1.4$, support = 3) was ap-
137 plied to the reconstructed images. Otsu's method (Otsu, 1979) was used to automatically
138 perform clustering-based image thresholding to segment the grey-level images into ice
139 and air phase. Morphological properties in the two-phase system were determined based
140 on the geometry obtained by the micro-CT. The segmented data were used to calculate a
141 triangulated ice matrix surface and tetrahedrons inscribed into the ice structure. Morpho-
142 logical parameters such as porosity (ε) and specific surface area (SSA) were then calcu-
143 lated. The opening size distribution with spherical structuring elements on the micro-CT
144 scans was used to estimate the mean pore size (d_p) (Haussener et al., 2012). The effec-
145 tive permeability was calculated using the finite volume technique CFD (Computational
146 Fluid Dynamics simulation software from ANSYS) by solving the continuity and Na-
147 vier–Stokes equations (Zermatten et al., 2011, 2014) for laminar flow

$$148 \quad \nabla p = -\frac{\mu}{K} u_D - F \rho u_D^2 - \frac{\gamma \rho^2}{\mu} u_D^3 \quad (1)$$

149 where p is the pressure, μ is the dynamic viscosity of the fluid and u_D its superficial ve-
150 locity, ρ is the fluid density, K is the permeability, F is the Dupuit-Forchheimer coeffi-
151 cient, and γ is a dimensionless factor. The first term is the result of viscous effects, pre-
152 dominant at low velocities, whereas the second and third terms describe the inertial ef-
153 fects, which become important at higher fluid velocities. As the viscous effect was still
154 the dominant case ($\text{Re} \approx 1$) in the experiment, only permeability K was considered for
155 further discussions. A grid convergence study based on the pressure drop (Zermatten et
156 al., 2014) was carried out to find the optimal representative elementary volume (REV)
157 ($6.0 \times 6.0 \times 3.0 \text{ mm}^3$). An in-house tetrahedron-based mesh generator (Friess et al.

2013) was used to create the computational grid on the segmented data. The computational domain consisted of a square duct containing a sample of snow. The boundary conditions consisted of uniform inlet velocity, temperature and outlet pressure, constant wall temperature at the solid-fluid interface, and symmetry of the sample at the lateral duct walls. The square duct was 5 times the length of the sample to ensure a fully developed velocity profile at the entrance of the snow sample (Fig. 2). The largest mesh element length was 0.153 mm and the smallest possible mesh element measured 9.56 μm , with average 60 million volume elements for each segmented snow sample.

3. Results and Discussion

The discussions of the observed results are only based on the investigated volume. Influences of the flow on the base, top and lateral boundaries of the overall sample were not considered due to lack of structural observations.

A representative temporal temperature profile of the snow sample for both laboratory temperatures of $T_{\text{lab}} = -8\text{ }^{\circ}\text{C}$ and $-15\text{ }^{\circ}\text{C}$ is shown in Figure 3. Variations in temperature up to $1.7\text{ }^{\circ}\text{C}$ and $1.4\text{ }^{\circ}\text{C}$ were due to heat dissipated by the X-ray tube and temperature fluctuations inside the cold laboratory (Ebner et al., 2014). A longer sintering duration at $-5\text{ }^{\circ}\text{C}$ of the snow for experiment ‘sa3’ and ‘sa4’ was used to increase the mean thickness of the ice matrix. This avoided the destruction of the snow structure due to shear stresses caused by the airflow. The structural analysis of the snow samples was conducted on the complete tomography domain ($7.2 \times 7.2 \times 7.2\text{ mm}^3$). A smaller sub-set of $110 \times 42 \times 110$ voxels ($2 \times 0.75 \times 2\text{ mm}^3$) was selected to visualize the 3D evolution (Fig. 4). It showed no significant change in the grain shape, even for different airflow velocities, and only a slight rounding and coarsening was seen for experiments ‘sa1’ and ‘sa2’. A strong translation effect due to settling of sub-layering snow was visible for ‘sa1’ and ‘sa2’. The initial ice matrix didn’t change with time; only coarsening processes on the ice grain surface were observed (Fig. 5). Sublimation of 4.5 % and 4.9 % of the ice matrix and deposition of 4.1 % and 5.9 % on the ice matrix were observed for ‘sa3’ and ‘sa4’ (Fig. 6). The data were extracted by superposition of vertical cross-sections at 0 and 96 hours with an uncertainty of 6 %. The mass sublimated preferentially at locations of the ice grain with low radii due to Kelvin-effect and was relocated on the grain leading to a smoothing of the ice grain. Our observed results were supported

189 by the vapour-pressure map simulated by Brzoska et al. (2008) and the applied airflow
190 velocity did not affect the relocation process.

191 The well-sintered snow showed very little settling under its own weight (Kaempfer
192 and Schneebeli, 2007) and, consequently, no significant change in porosity was ob-
193 served. This supports the hypothesis that further densification is limited by coarsening
194 kinetics (Kaempfer and Schneebeli, 2007, Schleef et al., 2013). A spatially constant po-
195 rosity distribution at $t = 0$ days and $t = 4$ days is seen in Fig. 7. Thus, spatial change in
196 the flow field due to different interfacial velocities can be neglected. Consequently, Pe
197 was constant with time, and therefore the advective and diffusive mass transfer regime.
198 The average deviation between $t = 0$ days and $t = 4$ days was 0.5%, 1.8%, 0.5% and
199 0.5% for ‘sa1’, ‘sa2’, ‘sa3’ and ‘sa4’.

200 Our segmented 3D-data accurately reproduced the original snow sample and the
201 temporal porosity distribution confirmed that no settling and densification occurred in
202 the investigated volume (Fig. 8). The gravimetric porosity $\varepsilon_{\text{grav}}$ at the beginning and at
203 the end of each experiment was measured by weighing. The measured density values
204 were converted to porosity ($\varepsilon_{\text{grav}} = 1 - \rho_s / \rho_{\text{ice}}$), and compared to the value of porosity com-
205 puted by DPLS on the micro-CT geometry. The computed values differed from the
206 measured ones by 1.4% and 0.1% at the beginning and 4.1% and 2.3% at the end for
207 experiments ‘sa3’ and ‘sa4’.

208 The qualitative progression of the spatial SSA of the scanned snow height for four
209 discs of $7.2 \times 7.2 \times 1.8 \text{ mm}^3$ (Fig. 9) did not change significantly with height. This sug-
210 gested that the snow properties were homogeneous throughout the sample and duration
211 of the experiments. The slight decrease of the spatial SSA for experiment ‘sa4’ is ex-
212 plained by the distribution not initially being completely homogeneous.

213 The coarsening process led to a decrease of the SSA over time (Fig. 10), which was
214 higher for group ‘sa1’ and ‘sa2’ compared to ‘sa3’ and ‘sa4’. The difference was caused
215 by the 34% lower initial SSA of group ‘sa3’ and ‘sa4’. Applying the theories developed
216 by Legagneux et al. (2004) and Legagneux and Domine (2005), the evolution of SSA of
217 the ice matrix could be modelled well. The model proposed is given by Legagneux and
218 Domine (2005)

219

$$\text{SSA} = \text{SSA}_0 \left(\frac{\tau}{\tau + t} \right)^{1/n} \quad (2)$$

220 where SSA_0 is the initial SSA at time $t = 0$, n is the growth exponent, and τ a parameter
221 related to grain growth and a form factor. Table 2 shows the fitted parameters and the
222 corresponding normalized root-mean square error (NRMSE) for each experiment. Equa-
223 tion (2) fits the data of each experiment well with an average NRMSE < 0.21 . The com-
224 puted fit of the SSA is shown in Figure 8. Equation (2) gives a very qualitative estima-
225 tion on the real mechanism occurring in the snow. This model is based on the physical
226 processes involved in Ostwald ripening (Ratke and Voorhees, 2002). Ostwald ripening
227 describes the coarsening of solid particles with a given size distribution, considering
228 disconnected grains that do not undergo settling. The driving force in the model is the
229 reduction of the SSA and the model hypothesis is based on the concept that mass trans-
230 fer occurs by sublimation due to curvature effects, transport through the gas phase and
231 deposition. Theoretically, the growth exponent n is approximately 2 when surface pro-
232 cesses are rate limiting and 3 when diffusion is rate limiting. Experiment ‘sa1’ and ‘sa2’
233 had a higher value of n , indicating a strong coarsening process due to sintering and that
234 surface processes were rate limiting (Legagneux et al., 2004; Legagneux and Domine,
235 2005). Experiment ‘sa1’ and ‘sa2’, and ‘sa3’ and ‘sa4’ had similar fitting parameters
236 and a low value of n , suggesting that surface effects were rate limiting (Legagneux et al.,
237 2004; Legagneux and Domine, 2005). The lower value of n for experiment ‘sa3’ and
238 ‘sa4’ was due to the longer sintering time of 27 days at $-5\text{ }^\circ\text{C}$ before the experiments were
239 started leading to a very little change in the microstructure of the snow. When the sinter-
240 ing times of 13 and 27 days were included in the model, the fitting parameters indicated
241 a consistent growth exponent n for each experiment (Table 3) and a good agreement
242 with the theory. They expressed strong coarsening and surface processes for each exper-
243 iment. Notice, Eq. (2) extremely depends on the initial state, which is well illustrated by
244 the large difference obtained for n values of ‘sa3’ and ‘sa4’ between Tables 2 and 3.
245 Concluding, the calculated values indicated that surface processes caused the limiting
246 rate rather than the diffusion step and no significant influence of advective transport
247 could be observed.

248 The effect of decreasing SSA on the permeability was not elucidated in our experi-
249 ments. A SSA decrease of at least 5% in the experiments could not be reproduced in the
250 permeability. However, the computational uncertainty up to 16% (Zermatten et al.,
251 2014) in the permeability is still in the range to cover the correlation between SSA and
252 permeability. The effect of increasing airflow velocity had no influence on the flow

253 characteristics (Fig. 11). The temporal evolution of permeability for experiment ‘sa2’
254 showed a decrease of 8% for the first 40 hours and remained constant afterwards. Exper-
255 iments ‘sa1’, ‘sa3’ and ‘sa4’ showed no significant change in the permeability, which is
256 consistent with the negligible change in density. The average fluctuations of the perme-
257 ability K between each time step and the slight decrease at the beginning in ‘sa2’
258 showed small differences that were below the precision of the numerical method with an
259 uncertainty up to 16% (Zermatten et al., 2014). Only the first time step of ‘sa3’ showed
260 a particularly high difference of 17.3%, but neither the porosity nor SSA showed signifi-
261 cant differences reflecting this value. This difference could therefore be due to an error
262 during the measurement or during the meshing procedure.

263

264 **4. Summary and conclusions**

265 Four isothermal metamorphism experiments of snow under saturated advective air-
266 flow were performed, each with duration of four days. The effects of the main transport
267 processes, diffusion and advection, were analysed inside the pore space. The airflow ve-
268 locities were chosen based on the Peclet number. $Pe > 0.85$ for natural surface condi-
269 tions were not possible due to the destruction of the snow structure and is not frequent
270 in natural snowpacks due to the low airflow velocities in snow (Neumann, 2003, Col-
271 beck, 1997). Every 8 h the snow microstructure was observed by X-ray micro-
272 tomography. The micro-CT scans were segmented, and porosity and specific surface
273 area were calculated. Effective permeability was calculated in direct pore-level simula-
274 tions (DPLS) to analyse the flow characteristic.

275 The experimental observations supported the hypothesis that further densification
276 was limited by coarsening kinetics and further confirmed a constant porosity evolution
277 (Kaempfer and Schneebeli, 2007). Curvature caused sublimation of small ice grains and
278 ice structures with small curvature radii leading to a slight decrease in SSA. Compared
279 to rates typical for isothermal snow metamorphism, no enhancement of mass transfer
280 inside the pores of isothermal advection with saturated air was observed. Sublimation-
281 deposition caused by the Kelvin-effect was the limiting factor independently of the
282 transport regime in the pores.

283

284 **Acknowledgements**

285 The Swiss National Science Foundation granted financial support under project Nr.
286 200020-146540. The authors thank M. Jaggi and S. Grimm for technical support with
287 the measurements.

288

289 **References**

- 290 Adams, E. E. and Walters, D. J.: Fine structure layering in radiation recrystallized snow,
291 International Snow Science Workshop, Proceedings, Banff, 2014.
- 292 Albert, M. R. and Mc Gilvary, W. R.: Thermal effects due to air flow and vapour
293 transport in dry snow, *Journal of Glaciology*, 38, 274–281, 1992.
- 294 Albert, M. R.: Numerical experiments on firn ventilation with heat transfer, *Annals of*
295 *Glaciology*, 18, 161–165, 1993.
- 296 Albert, M. R., Shuman, C., Courville, Z., Bauer, R., Fahnestock, M., and Scambos, T.:
297 Extreme firn metamorphism: impact of decades of vapor transport on near-surface
298 firn at a low-accumulation glazed site on the east Antarctic plateau, *Annals of Glac-*
299 *iology*, 39, 73–78, 2004.
- 300 Alley, R. B., Saltzman, E. S., Cuffey, K. M., and Fitzpatrick, J. J.: Summertime for-
301 mation of Depth Hoar in central Greenland, *Geophysical Research Letters*, 17, 2393-
302 2396, 1990.
- 303 Ansys, 2010: Ansys-CFX. In: A. Inc. (Ed.), (Canonsburg, PA).
- 304 Arnaud, L., Lipenkov, V., Barnola, J., Gay, M., and Duval, P.: Modelling of the densifi-
305 cation of polar firn: characterization of the snow-firn transition, *Annals of Glaciolo-*
306 *gy*, 26, 39–44, 1998.
- 307 Bader, H., Haefeli, R., Bucher, E., Neher, J., Eckel, C., and Thams, C.: Der Schnee und
308 seine Metamorphose, *Beitr. Geologie der Schweiz, Geotechnische Serie-Hydrologie*,
309 3, 1–313, 1939.
- 310 Brzoska, J.-B., Flin, F., and Barckicke, J.: Explicit iterative computation of diffusive
311 vapour field in the 3-D snow matrix: preliminary results for low flux metamorphism,
312 *Annals of Glaciology*, 48, 13-18, 2008.
- 313 Chen, S. and Baker, I.: Evolution of individual snowflakes during metamorphism, *Jour-*
314 *nal of Geophysical Research*, vol. 115, 1–9, 2010.
- 315 Clifton, A., Manes, C., Rüedi, J.-D., Guala, M., and Lehning, M.: On shear-driven venti-
316 lation of snow, *Boundary-Layer Meteorology*, 126, 249–261, 2008.
- 317 Colbeck, S. C.: Thermodynamics of snow metamorphism due to variations in curvature,
318 *Journal of Glaciology*, 26, 291–301, 1980.
- 319 Colbeck, S. C.: Air movement in snow due to wind-pumping, *Journal of Glaciology*, 35,
320 209–213, 1989.
- 321 Colbeck, S. C.: A review of sintering in seasonal snow, Technical Report, 97-10, Cold
322 Regions Research & Engineering Laboratory, Hanover, New Hampshire, 1997.
- 323 Colbeck, S. C.: Model of wind pumping for layered snow, *Journal of Glaciology*, 43,
324 60–65, 1997.
- 325 Colbeck, S. C.: Sintering in a dry snow cover, *Journal of Applied Physics*, 84, 4585–
326 4589, 1998.
- 327 Colbeck, S. C.: Sintering of unequal grains, *Journal of Applied Physics*, 89, 4612–4618,
328 2001.

329 Cunningham, J. and Waddington, E. D.: Air flow and dry deposition of non-sea salt sul-
330 phate in polar firn: paleoclimatic implications, *Atmospheric Environment*, 27A,
331 2943–2956, 1993.

332 Domine, F., M. Albert, T. Huthwelker, H.-W. Jacobi, A. A. Kokhanovsky, M. Lehning,
333 G. Picard, and W. R. Simpson: Snow physics as relevant to snow photochemistry,
334 *Atmos. Chem. Phys.*, 8, 171–208, 2008.

335 Fierz, C., Armstrong, R.L., Durand, Y., Etchevers, P., Greene, E., McClung, D.M.,
336 Nishimura, K., Satyawali, P.K. and Sokratov, S.A.: The International Classification
337 for Seasonal Snow on the Ground. IHP-VII Technical Documents in Hydrology
338 N°83, IACS Contribution N°1, UNESCO-IHP, Paris, 2009.

339 Gallet, J.-C., Domine, F., Savarino, J., Dumont, M., and Brun. E.: The growth of subli-
340 mation crystals and surface hoar on the Antarctic plateau, *The Cryosphere*, 8, 1205-
341 1215, 2014.

342 Ebner, P. P., Grimm, A. S., Schneebeli, M., and Steinfeld, A.: An instrumented sample
343 holder for time-lapse micro-tomography measurements of snow under advective
344 conditions, *Geoscientific Instrumentation Methods and Data Systems*, 3, 179–185,
345 2014.

346 Friess, H., Haussener, S., Steinfeld, A., and Petrasch, J.: Tetrahedral mesh generation
347 based on space indicator functions, *International Journal for Numerical Methods in*
348 *Engineering*, 93, 1040–1056, 2013.

349 German, R. M.: *Sintering Theory and Practice*, John Wiley, New York, 1996.

350 Gjessing, Y. T.: The filtering effect of snow. In: Oeschger, H., Ambach, W., Junge, C.
351 E., Lorius, C., and Serebryanny, L. (Eds.): *Isotopes and Impurities in Snow and Ice*
352 *Symposium*, 118, IASH-AISH Publication, Dorking, 199–203, 1977.

353 Grannas, A. M., *and 34 others*: An overview of snow photochemistry: evidence, mecha-
354 nisms and impacts, *Atmospheric Chemistry and Physics*, 7, 4329–4373, 2007.

355 Haussener, S., Gergely, M., Schneebeli, M., and Steinfeld, A.: Determination of the
356 macroscopic optical properties of snow based on exact morphology and direct pore-
357 level heat transfer modeling, *Journal of Geophysical Research*, 117, 1–20, 2012.

358 Hobbs, P. V. and Mason, B. J.: The sintering and adhesion of ice, *Philosophical Maga-*
359 *zine*, 9, 181–197, 1963.

360 Kaempfer, T. U. and Schneebeli, M.: Observation of isothermal metamorphism of new
361 snow and interpretation as a sintering process, *Journal of Geophysical Research*,
362 112, 1–10, 2007.

363 Kingery, W. D.: On the metamorphism of snow, in *International Geological Congress*,
364 *XXI Sesion*, Norden, Copenhagen, 81–89, 1960a.

365 Kingery, W. D.: Regelation, surface diffusion, and ice sintering, *Journal of Applied*
366 *Physics*, 31, 833–838, 1960b.

367 Kuroiwa, D.: A study of ice sintering, *Tellus*, 13, 252–259, 1961.

368 Legagneux, L. and Domine, F.: A mean field model of the decrease of the specific sur-
369 face area of dry snow during isothermal metamorphism, *Journal of Geophysical Re-*
370 *search*, 110, F04011, doi:10.1029/2004JF000181, 2005.

371 Legagneux, L., Taillandier, A. S., and Domine, F.: Grain growth theories and the iso-
372 thermal evolution of the specific surface area of snow, *Journal of Applied Physics*,
373 95, 6175–6184, 2004.

374 Legrand M. and Mayewski P.: Glaciochemistry of polar ice cores: A review, *Reviews of*
375 *Geophysics*, 35, 219–243, 1997.

- 376 Löwe, H., Spiegel, J. K., and Schneebeli, M.: Interfacial and structural relaxations of
377 snow under isothermal conditions, *J. Glaciology*, 57, 499–510, 2011.
- 378 McConnell, J. R., Bales, R. C., Stewart, R. W., Thompson, A. M., Albert, M. R., and
379 Ramos, R.: Physically based modelling of atmosphere-to-snow-to-firn transfer of
380 H_2O_2 at the South Pole, *Journal of Geophysical Research*, 103, 10561–10570, 1998.
- 381 Maeno, N. and Ebinuma, T.: Pressure sintering of ice and its implication to the densifi-
382 cation of snow at polar glaciers and ice sheets, *Journal of Physical Chemistry*, 87,
383 4103–4110, 1983.
- 384 Neumann, T. A.: Effects of firn ventilation on geochemistry of polar snow, (PhD thesis,
385 University of Washington), 2003.
- 386 Neumann, T. A. and Waddington, E. D.: Effects of firn ventilation on isotopic ex-
387 change, *Journal of Glaciology*, 50, 183–194, 2004.
- 388 Neumann, T. A., Albert, M. R., Engel, C., Courville, Z., and Perron, F.: Sublimation
389 rate and the mass transfer coefficient for snow sublimation, *International Journal of*
390 *Heat and Mass Transfer*, 52, 309–315, 2009.
- 391 Otsu, N.: A Threshold Selection Method from Gray-Level Histograms, *IEEE Transac-*
392 *tions on Systems Man and Cybernetics*, 9, 62–66, 1979.
- 393 Pinzer, B. R. and Schneebeli, M.: Breeding snow: an instrumented sample holder for
394 simultaneous tomographic and thermal studies, *Measurement Science and Technol-*
395 *ogy*, 20, 1–9, 2009.
- 396 Pinzer, B. R., Schneebeli, M., and Kaempfer, T. U.: Vapor flux and recrystallization
397 during dry snow metamorphism under a steady temperature gradient as observed by
398 time-lapse micro-tomography, *The Cryosphere*, 6, 1141–1155, 2012.
- 399 Ratke, L. and Voorhees, P. W.: *Growth and Coarsening*, Springer, ISBN 3-540-42563-2,
400 2002.
- 401 Schleef, S. and Löwe, H.: X-ray microtomography analysis of isothermal densification
402 of new snow under external mechanical stress, *Journal of Glaciology*, 59, 233–243,
403 2013.
- 404 Schleef, S., Jaggi, M., Löwe, H., and Schneebeli, M.: Instruments and Methods: An im-
405 proved machine to produce nature-identical snow in the laboratory, *Journal of Glac-*
406 *iology*, 60, 94–102, 2014.
- 407 Schneebeli, M. and Sokratov, S.: Tomography of temperature gradient metamorphism
408 of snow and associated changes in heat conductivity, *Hydrological Processes*, 3665,
409 3655–3665, 2004.
- 410 Severinghaus, J. P., Albert, M. R., Courville, Z. R., Fahnestock, M. A., Kawamura, K.,
411 Montzka, S. A., Muehle, J., Scambos, T. A., Shields, E., Shuman, C. A., Suwa, M.,
412 Tans, P., and Weiss, R. F.: Deep air convection in the firn at a zero-accumulation
413 site, central Antarctica, *Earth and Planetary Science Letters*, 293, 359–367, 2010.
- 414 Sowers, T., Bender, M., Raynard, D., and Korotkevich, Y. S.: $\delta^{15}\text{N}$ in air trapped in po-
415 lar ice: a tracer of gas transport in the firn and a possible constraint on ice age-gas
416 age differences, *Journal of Geophysical Research*, 97, 15683–15697, 1992.
- 417 Stössel, F., Guala, M., Fierz, C., Manes, C., and Lehning M.: Micrometeorological and
418 morphological observations of surface hoar dynamics on a mountain snow cover,
419 *Water Resources Research*, 46, 1–11, 2010.
- 420 Sturm, M. and Johnson, J. B.: Natural convection in the subarctic snow cover, *Journal*
421 *of Geophysical Research*, 96, 11657–11671, 1991.
- 422 Vetter, R., Sigg, H. M., Singer, D., Kadau, H. J., Herrmann, and M. Schneebeli, Simu-
423 lating isothermal aging of snow, *EPL (Europhysics Lett.)*, 89(2), 26001,
424 doi:10.1209/0295-5075/89/26001, 2010.

- 425 Waddington, E. D., Cunningham, J., and Harder, S. L.: The effects of snow ventilation
426 on chemical concentrations. In: Wolff, E. W. and Bales, R. C. (Eds.), *Chemical Ex-*
427 *change Between the Atmosphere and Polar Snow*, NATO ASI Series, 43, Springer,
428 Berlin, 403–452, 1996.
- 429 Wang, X. and Baker, I.: Evolution of the specific surface area of snow during high-
430 temperature gradient metamorphism, *Journal of Geophysical Research Atmospheres*,
431 vol. 119, 13690 – 13703, 2014.
- 432 Zermatten, E., Haussener, S., Schneebeli, M., and Steinfeld, A.: Instruments and Meth-
433 ods: Tomography-based determination of permeability and Dupuit-Forchheimer co-
434 efficient of characteristic snow samples, *Journal of Glaciology*, 57, 811–816, 2011.
- 435 Zermatten, E., Schneebeli, M., Arakawa, H., and Steinfeld, A.: Tomography-based de-
436 termination of porosity, specific area and permeability of snow and comparison with
437 measurements, *Cold Regions and Technology*, 97, 33–40, 2014.
- 438
- 439

440 **Table 1:** Morphological and flow characteristics of the experiments: Volume flow (\dot{V}),
 441 corresponding Peclet number (Pe), Reynolds number (Re), initial superficial velocity in
 442 snow ($u_{D,0}$), initial snow density (ρ_0), initial porosity (ε_0), specific surface area (SSA_0),
 443 initial pore diameter (d_p), temperature in the cold laboratory (T_{lab}), and the sintering time
 444 of the snow.

445

Name	\dot{V} litre min ⁻¹	Pe –	Re –	$u_{D,0}$ m s ⁻¹	ρ_0 kg m ⁻³	ε_0 –	SSA_0 m ² kg ⁻¹	d_p mm	T_{lab} °C	Sintering time
sa1	–	–	–	–	229.25	0.75	46.6	0.22	-8.0	13 days at -15°C
sa2	0.36	0.05	0.07	0.004	201.74	0.78	43.7	0.27	-8.0	13 days at -15°C
sa3	3.0	0.47	0.6	0.04	320.95	0.65	28.7	0.24	-15.0	27 days at -5°C
sa4	5.0	0.85	1.1	0.06	265.93	0.71	28.0	0.29	-15.0	27 days at -5°C

446

447

448 **Table 2:** Values of the fitted growth rate τ and growth exponent n for the evolution of
 449 the SSA and the corresponding normalized root-mean square error (NRMSE).

450

Name	SSA_0 m ² kg ⁻¹	τ –	n –	NRMSE –
sa1	46.7	632.9	2.10	0.01
sa2	43.6	721.2	2.15	0.04
sa3	27.8	14400	0.32	0.14
sa4	27.8	17380	0.39	0.21

451

452 **Table 3:** Values of the fitted growth rate τ and growth exponent n for the evolution of
 453 the SSA including the sintering time of 13 and 27 days, and the corresponding normal-
 454 ized root-mean square error (NRMSE).

455

Name	SSA_0 m ² kg ⁻¹	τ –	n –	NRMSE –
sa1	64.4	320.9	2.10	0.01
sa2	56.8	409.1	2.15	0.04
sa3	34.5	1229	2.0	0.15
sa4	36.0	1063	1.91	0.27

456

457 **Figure captions**

458 **Fig. 1.** Schematic of the experimental setup and the sample holder. A thermocouple
459 (TC) and a humidifier sensor (HS) inside the humidifier measured the air-
460 flow conditions. Two thermistors (NTC) close to the snow surface measured
461 the inlet and outlet temperature of the airflow (Ebner et al., 2014).

462 **Fig. 2.** Schematic of the computational domain with an enlarged subsample of
463 snow. In the snow sample, the dark gray part represents the ice, whereas the
464 mesh is built in the pore space.

465 **Fig. 3.** A typical temperature profile for experiment ‘sa1, sa2’ and ‘sa3, sa4’. The
466 temperature rise was caused by the X-ray tube and fluctuations inside the
467 cold laboratory (Ebner et al., 2014). The accurateness of the isothermal con-
468 ditions between the top and base of the sample throughout the experiment is
469 less than 0.2 °C which is still in the uncertainty of the thermistors ± 0.2 K
470 (Ebner et al., 2014).

471 **Fig. 4.** Evolution of the 3-D structure of the ice matrix during isothermal metamor-
472 phism under advective conditions. Experimental conditions (from left to
473 right) at different measurement times from beginning to the end (top to bot-
474 tom) of the experiment. The shown cubes are $110 \times 42 \times 110$ voxels ($2 \times$
475 0.75×2 mm³) large.

476 **Fig. 5.** Residence time of ice particles within in a slice (5.7×5.7 mm²) parallel to
477 the flow direction for a) ‘sa3’ and b) ‘sa4’ by overlapping time-lapse tomog-
478 raphy pictures. The period of 8 h was sufficiently short to calculate the resi-
479 dence time of each ice voxel with an uncertainty of 6 %.

480 **Fig. 6.** Superposition of vertical cross-section parallel to the flow direction at time 0
481 and 96 hours for (a) ‘sa3’ and (b) ‘sa4’. Sublimation and deposition of water
482 vapor on the ice grain were visible with an uncertainty of 6 %.

483 **Fig. 7.** Spatial porosity profile of the scanned area at the beginning and at the end of
484 each experiment. The spatial variability within the reconstructed volume
485 was measured in four discs of $7.2 \times 7.2 \times 1.8$ mm³.

486 **Fig. 8.** Evolution of the porosity over time obtained by triangulated structure sur-
487 face method and the measured gravimetric density (ϵ_{grav}) at the beginning
488 and at the end of ‘sa3’ and ‘sa4’.

- 489 **Fig. 9.** Spatial SSA profile of the scanned area at the beginning and at the end of
490 each experiment. The spatial variability within the reconstructed volume
491 was measured in four discs of $7.2 \times 7.2 \times 1.8 \text{ mm}^3$.
- 492 **Fig. 10.** Temporal evolution of the specific surface area, SSA, of the ice matrix ob-
493 tained by triangulated structure surface method. The computed fit is of the
494 form $SSA(t) = SSA_0 \left(\frac{\tau}{\tau+t} \right)^{\frac{1}{n}}$.
- 495 **Fig. 11.** Temporal evolution of the effective permeability by applying DPLS with an
496 uncertainty of 16 % (Zermatten et al., 2014).
497

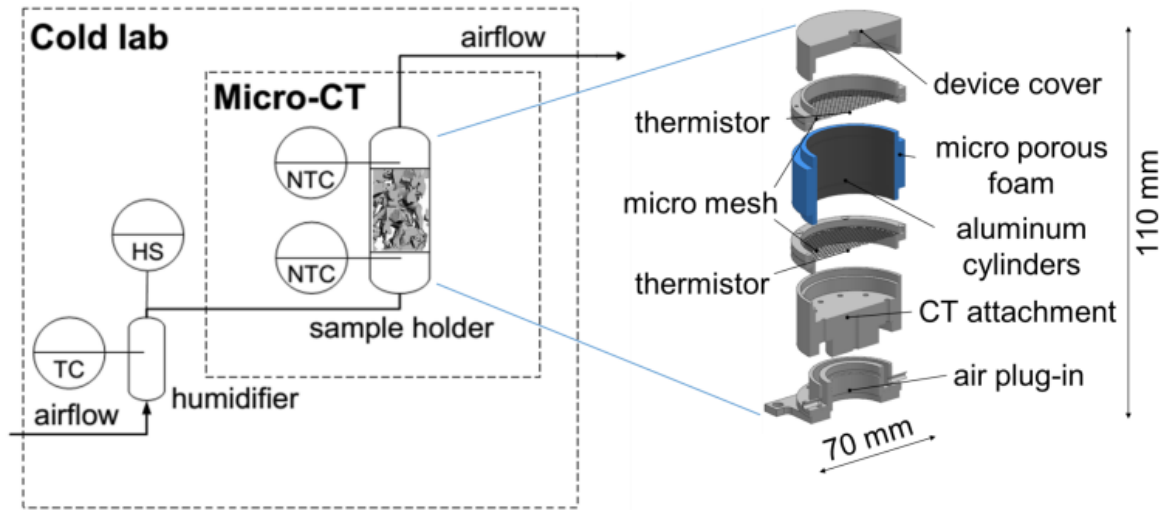
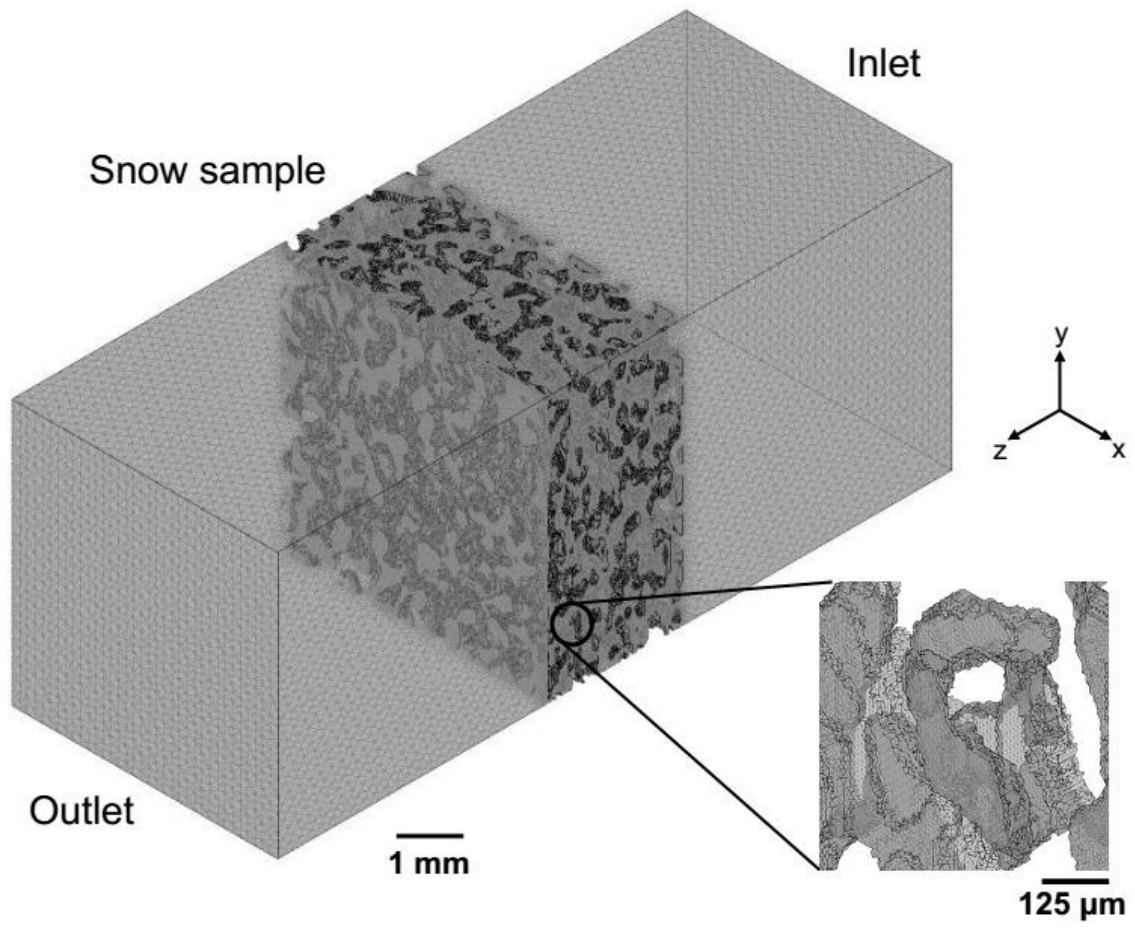


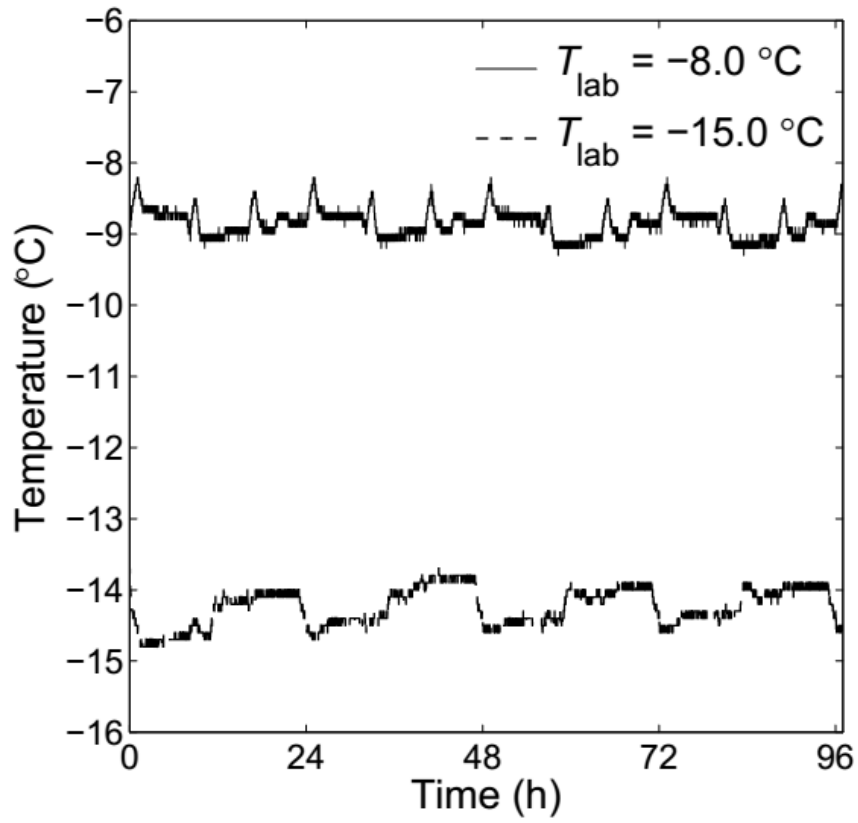
Fig. 1

498
499
500



501
502
503

Fig. 2



504
505

Fig. 3

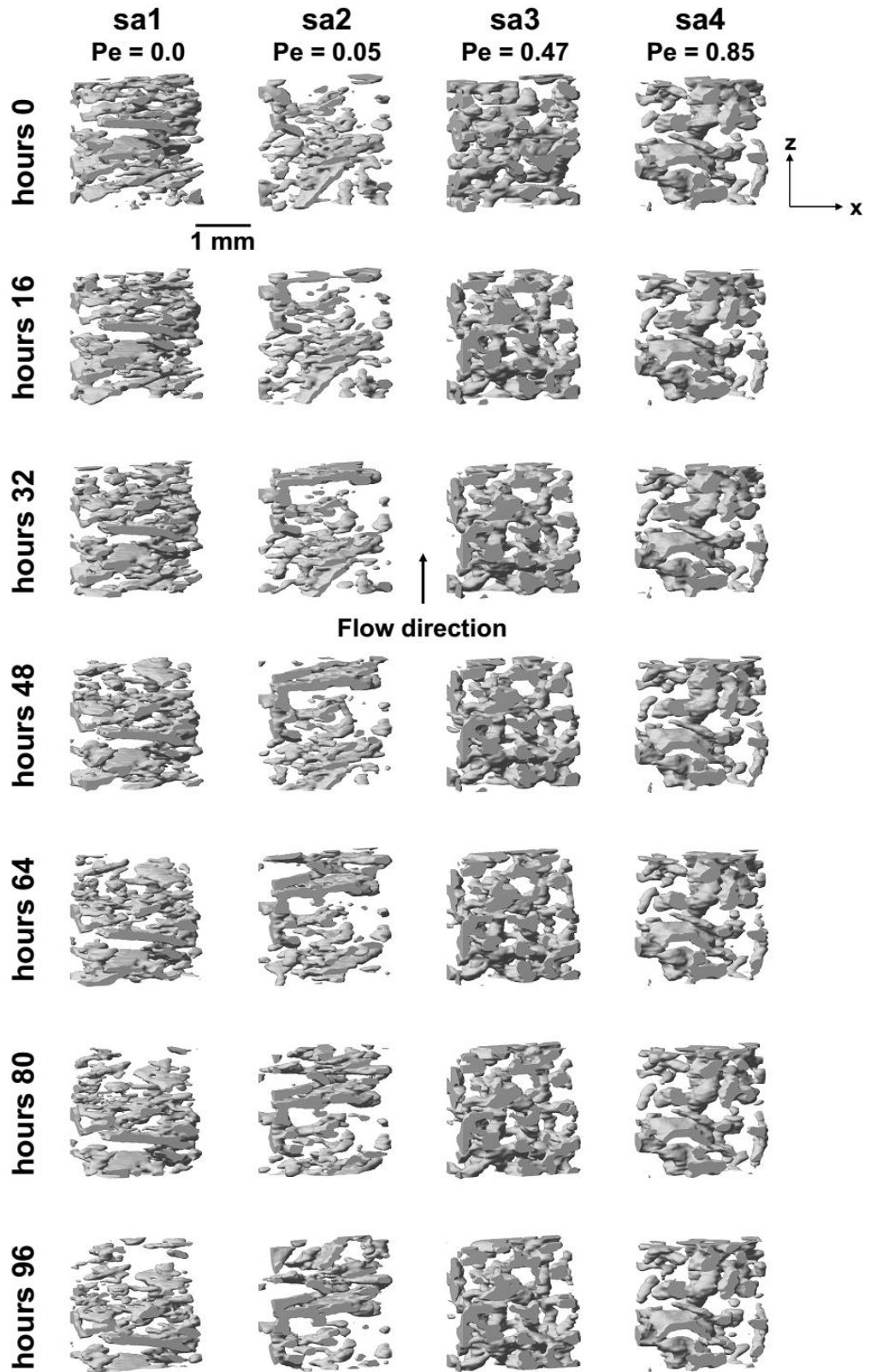
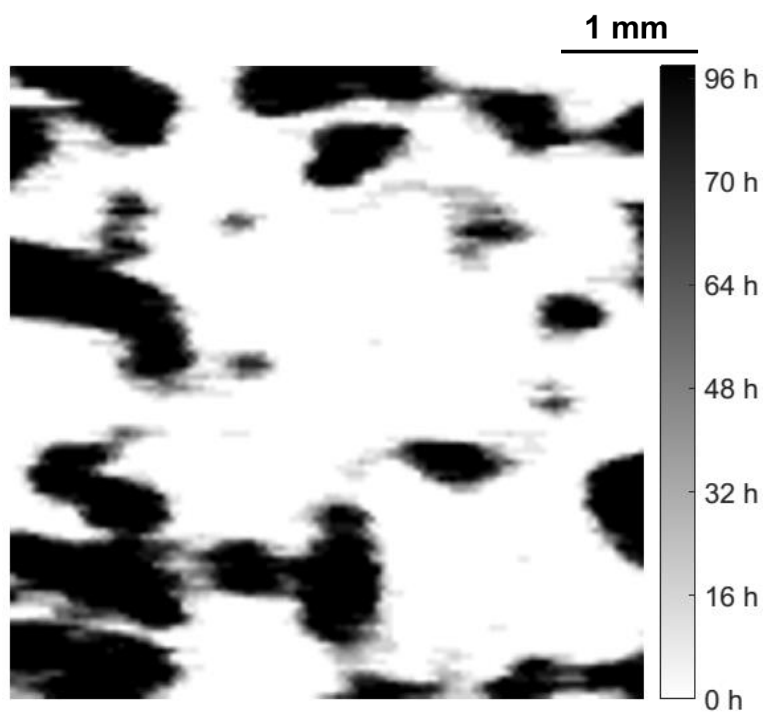


Fig. 4

506
507



508
509

Fig. 5 a)

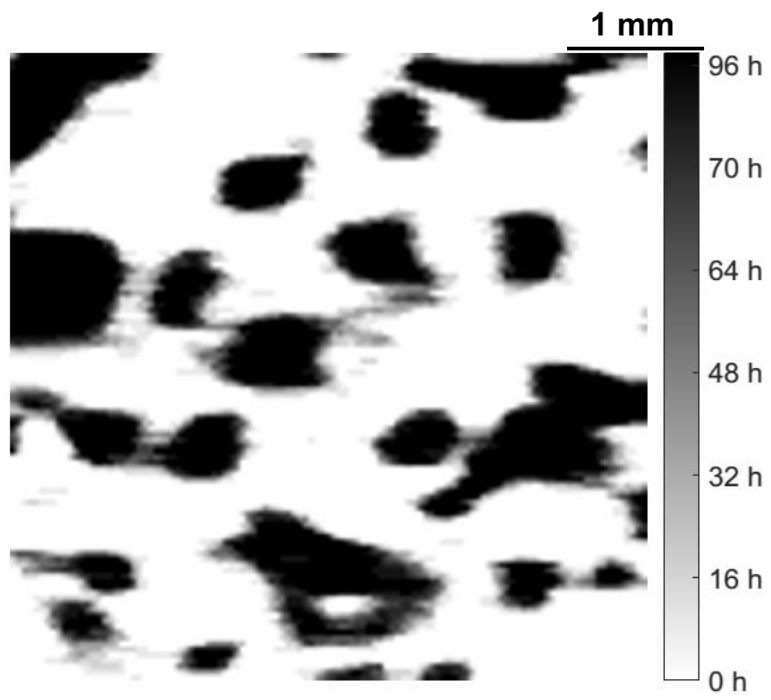


Fig. 5 b)

510
511
512

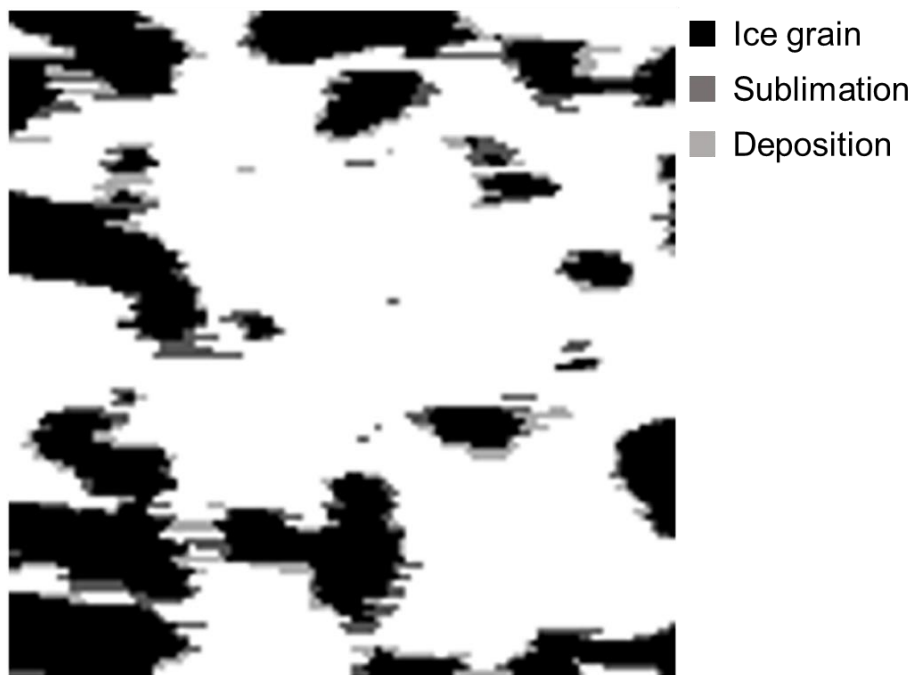
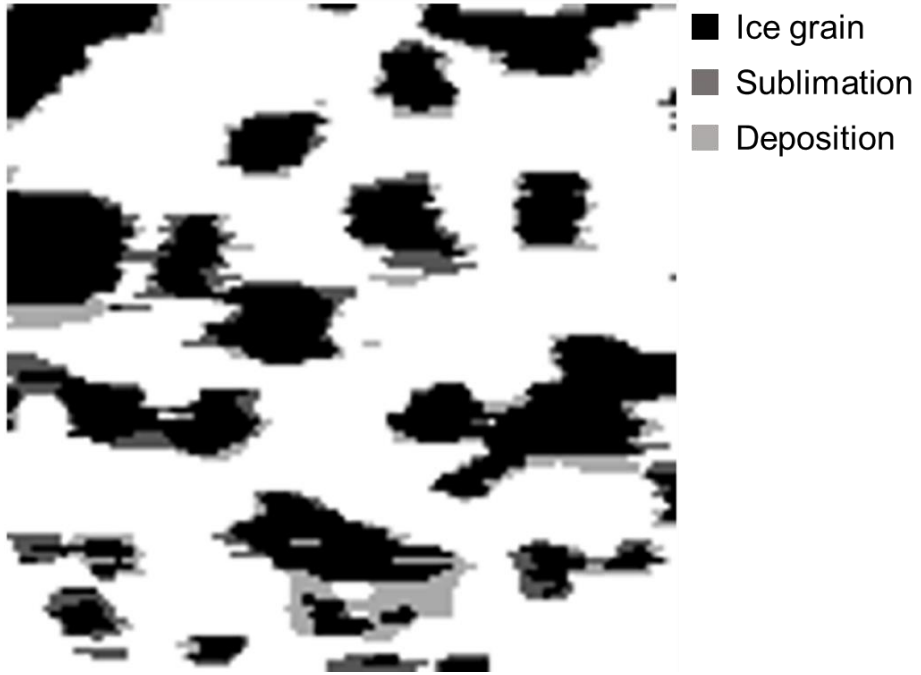


Fig 6 a)

513
514
515



516
517
518

Fig. 6 b)

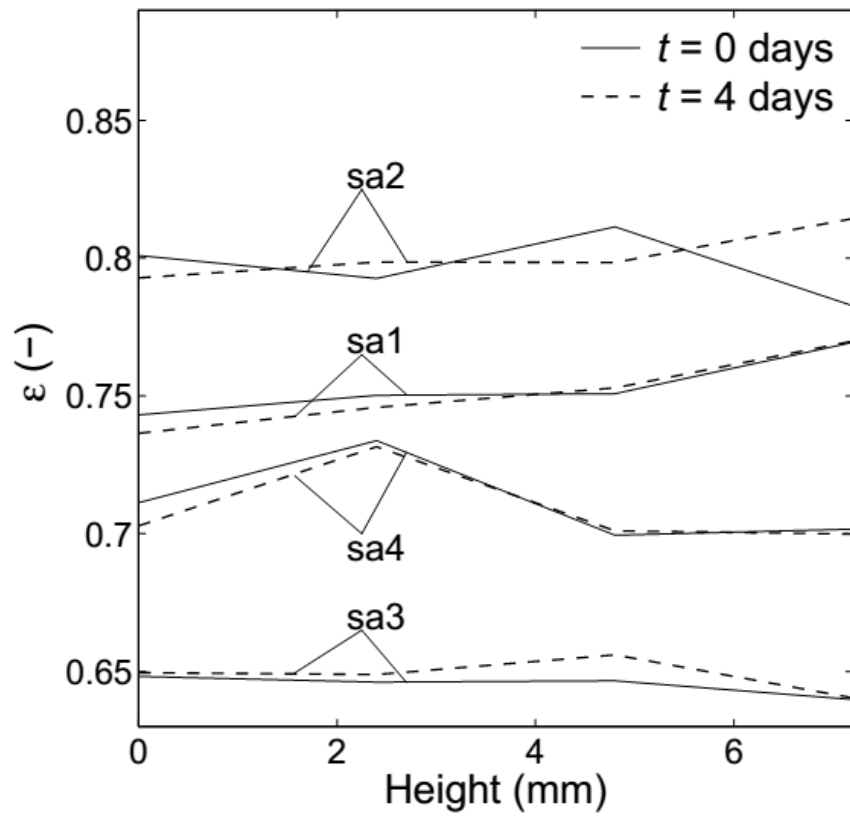


Fig. 7

520
521
522

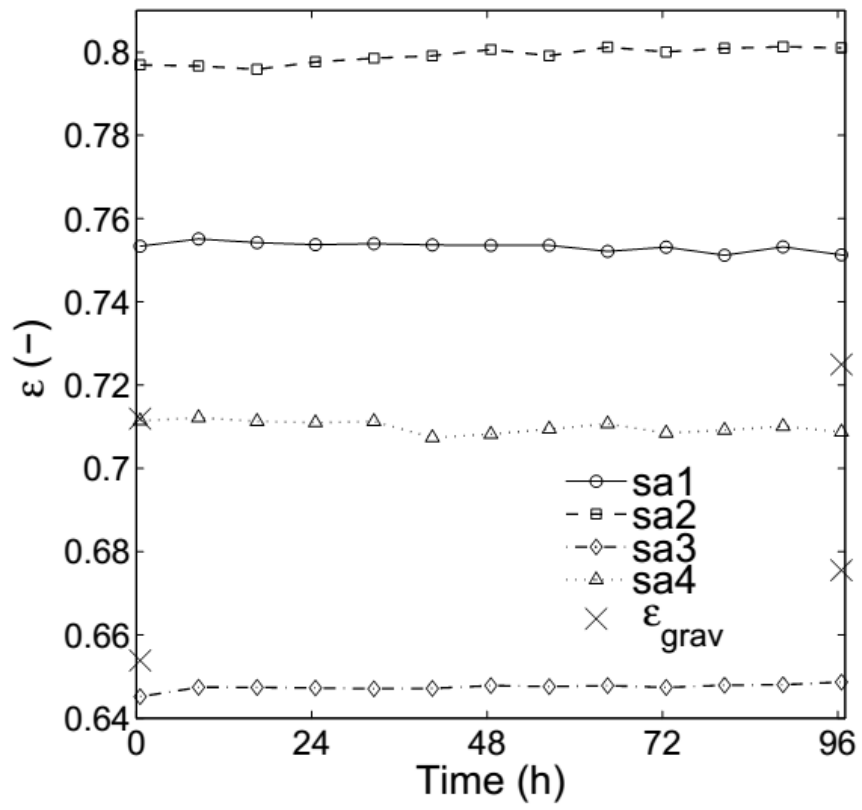


Fig. 8

523
524
525

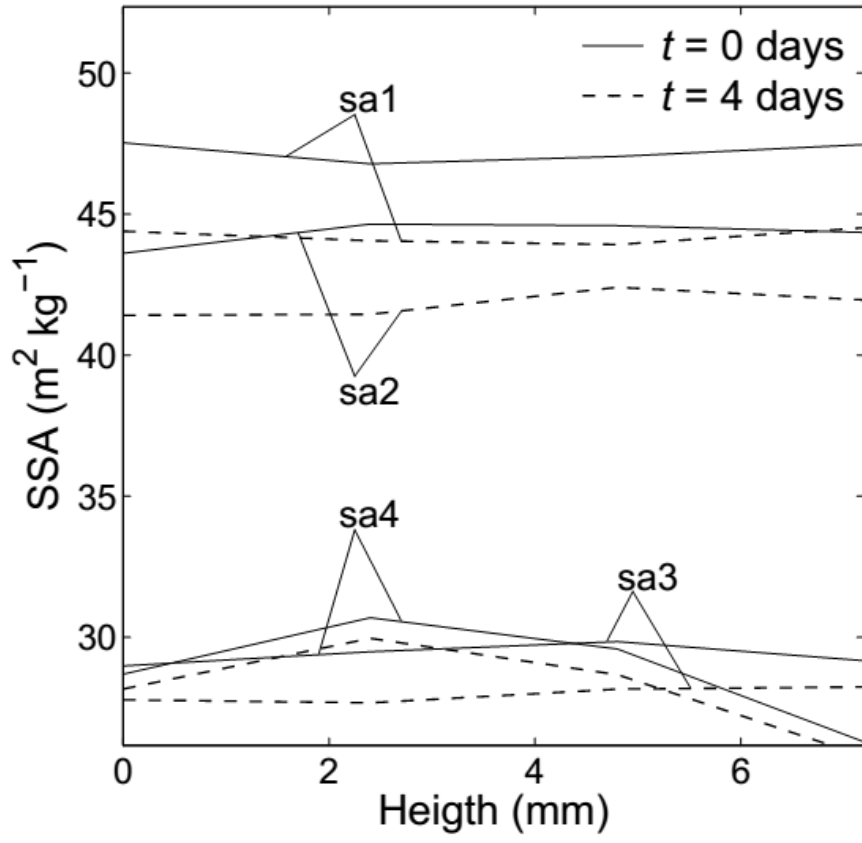
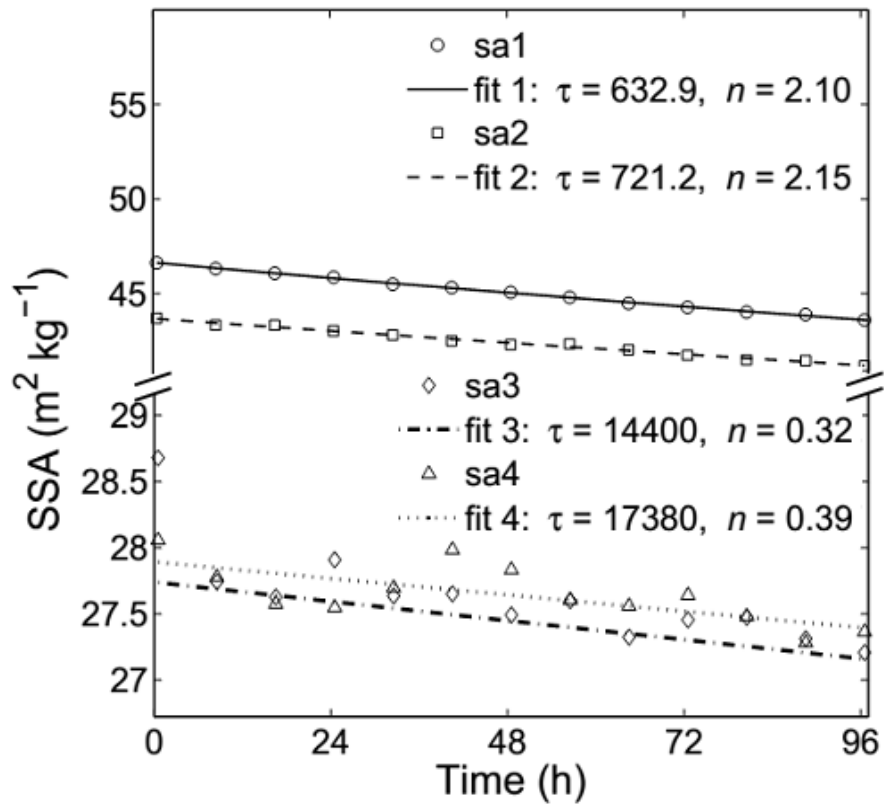


Fig. 9

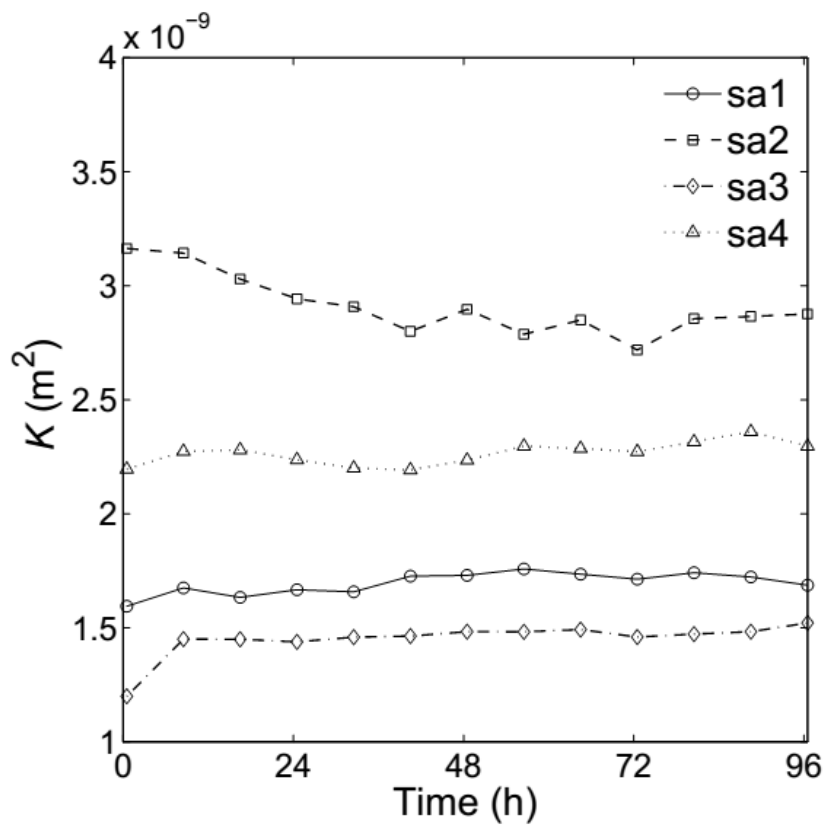
526
527
528
529



530
531
532

Fig. 10

533
534



535
536

Fig. 11